

Measurement of the x-ray mass attenuation coefficient of silver using the x-ray-extended range technique

C Q Tran¹, C T Chantler¹, Z Barnea¹, M D de Jonge¹, B B Dhal¹,
C T Y Chung¹, D Paterson² and J Wang²

¹ School of Physics, University of Melbourne, VIC 3010, Australia

² XOR, APS, Argonne National Laboratory, 9700 South Cass Avenue, Argonne, IL 60439, USA

E-mail: tran@physics.unimelb.edu.au

Received 27 August 2004, in final form 12 November 2004

Published 17 December 2004

Online at stacks.iop.org/JPhysB/38/89

Abstract

We used the x-ray-extended range technique to measure the x-ray mass attenuation coefficients of silver in the 15–50 keV energy range with a level of uncertainty between 0.27% and 0.4% away from the K-edge. The imaginary part of the atomic form factor of silver was derived by subtracting the scattering component from the measured total mass attenuation coefficients. Discrepancies between the measured mass attenuation coefficients and alternative theoretical predictions are discussed.

1. Introduction

There have been continuing efforts to address discrepancies between current mass attenuation coefficient measurements and computations [1–5]. Discrepancies between theories and experiments have been orders of magnitude larger than claimed uncertainties and have stimulated direct investigations of conditions required for accurate measurements [6, 7]. Recent reviews have discussed the overall status and detailed difficulties with available solutions [8–11]. This disagreement occurs for most elements across the intermediate energy range. However, major problems arise particularly with higher Z elements. Recently, we have demonstrated that the x-ray-extended range technique (XERT) [12–15], which uses multiple specimens over extended ranges in energy, is capable of identifying major sources of systematic errors affecting attenuation measurements.

In the self-consistent field method, atomic electrons are assumed to move in an average central potential due to the nuclear field and the average contribution from other atomic electrons. For higher Z elements, correlation between atomic electrons becomes more significant, and contributions from outer-shell electrons are calculated at lower accuracies due to the errors accumulated from the calculations for inner-shell electrons. Low-energy calculations of atomic form factors for higher Z elements are therefore less reliable.

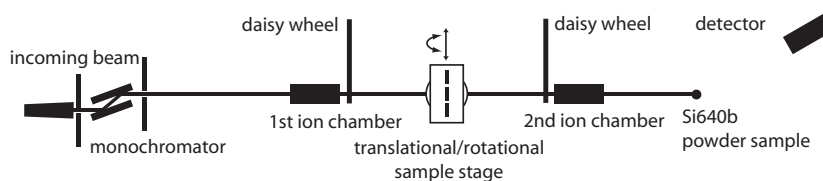


Figure 1. Experimental set-up: APS, beamline 1BM: silver 15–50 keV. The two daisy wheels were required to quantify the scattering contribution in this high energy range. Also, thick absorbers were mounted on the rims of these wheels for the investigation of harmonic components present in the beam.

Atomic form factors can be determined experimentally by various methods, such as interferometry, total external reflection, refraction through prisms, fitting diffraction profiles, or by direct measurement of attenuation [1–7, 12–15]. Each method has particular advantages and disadvantages [16]. Determination of the real component of the atomic form factor involves the use of Bragg diffraction or of the coherent (or elastic or Rayleigh) scattering process. Calculations of this scattering process can be found in [17]. The imaginary component of the atomic form factor, which is proportional to the photoelectric absorption coefficient, can be determined very accurately from measurements of attenuation but requires correction for scattering and fluorescence contributions [18].

Since heavy elements are more absorbing, experimental work dealing with these elements requires the use of quite thin foils, especially at energies of interest to crystallography. Accordingly, accurate determination of the local thickness of specimens becomes much more challenging. This is one of the main reasons for the dearth of good quality data for heavy elements in the literature. At high energies, the contributions from scattering processes become commensurate with those from the photoelectric absorption. Accurate allowance for scattering is therefore required in order to extract the photoelectric component from the measured mass attenuation coefficients.

Our earlier work targeted low to medium Z elements at relatively low energies. However, the techniques of these experiments are not entirely adequate for experiments with high Z elements, especially at higher energies. In particular, the investigation of the scattering contribution, which is more significant in this higher energy range, requires some modification of the original experimental set-up.

This paper presents the results of our measurement of the x-ray mass attenuation coefficient of silver in the 15–50 keV energy range. The level of the accuracy of the measurement (0.27%–0.4% away from the K-edge and up to 0.7% in the K-edge region) makes it possible to compare these results with alternative theoretical predictions. The imaginary part of the atomic form factor of silver was derived by subtracting the scattering component from the total attenuation coefficients and using the resultant photoelectric mass absorption coefficients in the optical theorem.

2. Experimental details

The experiment was conducted at the third-generation APS synchrotron radiation source, beamline 1BM [19]. Figure 1 shows the experimental arrangement [12, 14]. The beam was monochromatized by a double-reflection 400 silicon monochromator and was collimated to a $2 \times 2 \text{ mm}^2$ cross-section. The incident and attenuated intensities were detected by two ion chambers. The flow of nitrogen gas through the two ion chambers and the electronic settings were optimized for stability of the readings and for counting statistics [20].

The foils were mounted on a sample stage which was located 29.5 cm from both the ion chambers. We used high-purity foils (99.999%) supplied by the Goodfellow and ESPI companies. Three foils of different thicknesses, ranging from 12 μm to 275 μm , were used at each energy covering the attenuation range, $\ln(I_0/I)$, from 0.1 to 6.8. This large attenuation range was necessary to isolate and correct several experimental systematic effects [21]. Effects from the most dominant impurities of the foils (quoted as 4 ppm Cd, 2 ppm Ni and 1 ppm or less of Cu, Fe, Na and Zn) on the measurement were calculated to be insignificant.

The energy step sizes ranged from 200 eV to 400 eV (away from the edge) and from 5 eV to 50 eV (near the edge). We used a NIST standard Si640b powder sample ($a_0 = 5.430\,940(11)$ Å [22]) mounted on a 6-circle Huber stage to directly measure the energy of the beam at a number of energies. These energy measurements were used to calibrate the encoder readings of the angular positions of the monochromator in order to determine beam energies at which attenuation measurements were carried out.

In this experiment, we used two daisy wheels which were mounted between the sample stage and the ion chambers. The 16 aluminium foils mounted on the rim of the downstream daisy wheel were used to investigate the effective harmonic content of the beam [25]. Additionally, both daisy wheels had three circular apertures whose diameters were 3 mm, 6 mm and 16 mm. All three apertures were used in turn at each energy during the main attenuation measurement. By comparing the readings of the ion chambers and the corresponding $\ln(I_0/I)$ obtained with the three aperture sizes, contributions from fluorescence and scattering to the attenuation measurements can be determined [23, 18].

For this set-up with three attenuation foils and two daisy wheels, we developed macros (in the SPEC language) to automate the measurement sequence at each energy according to the following order: $H \rightarrow A_{\text{large}} F_1 \rightarrow A_{\text{large}} B_1 \rightarrow A_{\text{large}} F_2 \rightarrow A_{\text{large}} B_2 \rightarrow A_{\text{large}} F_3 \rightarrow A_{\text{medium}} F_3 \rightarrow A_{\text{medium}} B_2 \rightarrow A_{\text{medium}} F_2 \rightarrow A_{\text{small}} F_2 \rightarrow A_{\text{small}} B_1 \rightarrow A_{\text{small}} F_1 \rightarrow D$, where H indicates a measurement of harmonics using multiple foils mounted on the perimeter of the daisy wheel; the x in A_x can be large, medium, or small, and indicates which aperture size was used; F_i and B_i represent measurements with the i th foil and without a foil (referring to the two positions in the middle of the gaps between the foils, as shown in figure 1); D indicates a dark current measurement.

3. Detailed analysis

3.1. Sample thickness determination

The error in the determination of the ‘local’ thickness of the sample through which the beam actually passed is usually the dominant contribution to the final uncertainty of the result. We have therefore developed a technique which can accurately determine the local mass per unit area (ρt_{loc}) even of thin foils [24]. The technique essentially involves (i) the accurate determination of the local thickness of the thickest foils using a combination of weighing and measuring the foil area, two-dimensional mapping of the local thickness of the foil using a 1 μm resolution micrometer and two-dimensional mapping of the relative attenuation of the foils using the x-ray beam and (ii) scaling of the local thickness of the thinner foils to the thicker ones.

In this experiment, the local thicknesses of the three thickest foils, two of nominal thickness 275 μm (foils 275A and 275B, table 1) and the third of 100 μm (foil 100, table 1), were directly measured at a number of energies. The results of the six measurements of the local thickness of these three thickest foils are summarized in table 1.

Table 1. t_{nom} and t_{meas} represent the nominal and measured local thickness of the thickest foils used in the measurements, $\% \Delta_{t,\text{stat}}$ represents the percentage uncertainty in measured thickness due to counting statistics, $\% \Delta_t$ is the total percentage uncertainty in the measured thickness and column E lists the energies of the incident beam at which thickness measurements were carried out. Repeated measurements were carried out (foils 275B and 100) at various energies to check the accuracy of the procedure.

Foil	t_{nom} (μm)	t_{meas} (μm)	$\% \Delta_{t,\text{stat}}$ (%)	$\% \Delta_t$ (%)	E (keV)
275A	275	278.36	0.17	0.28	24.4
275B	275	276.89	0.18	0.21	22.8
275B	275	276.80	0.27	0.30	20.0
100	100	102.87	0.21	0.36	24.4
100	100	103.02	0.15	0.31	20.0
100	100	102.97	0.44	0.51	15.0

Table 2. Final results of the determination of the local thickness of the thickest foils used in the measurements. $\% \Delta_t$ is the final percentage uncertainty in the thickness determination, combining the results of repeated measurements listed in table 1, other columns have been defined in table 1.

Foil	t_{nom} (μm)	t_{meas} (μm)	$\% \Delta_t$ (%)	E (keV)
275A	275	278.36	0.28	24.4
275B	275	276.86	0.17	22.8 and 20
100	100	102.87	0.36	24.4
100	100	103.00	0.27	20 and 15

The detailed determinations of the local measured thickness, t_{meas} , and its total percentage uncertainty, $\% \Delta_t$, have been discussed elsewhere [24]. Contributions from counting statistics, $\% \Delta_{t,\text{stat}}$ which vary with the attenuation, are included. In this experiment, the statistical uncertainty is the dominant contribution to the total uncertainty $\% \Delta_t$ of the measured thicknesses. Due to time constraints, we took only one reading per point of the two-dimensional x-ray attenuation map. Repeated measurement would have further reduced this statistical error significantly.

Two independent two-dimensional x-ray mappings were carried out for foil 275B (second and third rows) and three for foil 100 (last three rows) at a number of energies and the results of the thickness determination were compared to test the accuracy of the thickness determination procedure. The two results for 275B (276.89 μm and 276.80 μm) are consistent within 0.03%. This is well within the uncertainty of the individual measurements and a strong confirmation of the reliability of the technique. The last two measurements of the 100 foil (103.02 $\mu\text{m} \pm 0.31\%$ and 102.97 $\mu\text{m} \pm 0.51\%$) are consistent within 0.05% and again show the robustness of the technique. The first measurement of the 100 foil, taken at 24.4 keV, is different from the mean of the other two by about 0.13%. This foil was removed and reinserted between the measurements; this may have resulted in the local foil thickness being somewhat different. Final results of the determination of the local thickness of these foils, calculated as the weighted mean of the repeated measurements, are summarized in table 2.

The local thicknesses of the other (thinner) foils used in the experiment were directly scaled against the thicknesses of the foils listed in table 2 using the thickness transfer scheme [24].

3.2. Effects of scattering and fluorescence

In the interpretation of attenuation coefficients in the intermediate x-ray energy range, the total mass attenuation coefficient of amorphous materials is often approximated as the sum of the photoelectric, Rayleigh and Compton scattering components:

$$[\mu/\rho]_{\text{tot}} = [\mu/\rho]_{\text{pe}} + [\mu/\rho]_{\text{R}} + [\mu/\rho]_{\text{C}}. \quad (1)$$

The measured mass attenuation coefficients $[\mu/\rho]_{\text{meas}}$ are then often assumed to be the total mass attenuation coefficients $[\mu/\rho]_{\text{tot}}$. The Rayleigh and Compton components, $[\mu/\rho]_{\text{R}}$ and $[\mu/\rho]_{\text{C}}$, are then subtracted from the measured attenuation coefficients $[\mu/\rho]_{\text{meas}}$ to obtain the photoelectric component $[\mu/\rho]_{\text{pe}}$ which is directly related to the imaginary part of the atomic form factor.

However, measurements of x-ray attenuation are also affected by secondary photons reaching the detectors. Secondary photons arise from scattering of incident photons by the absorbing material and the air path, and from the x-ray fluorescence produced in the absorber by the incident beam. The magnitude of the contribution of these effects depends on the x-ray optics, collimation, photon energy, detector response function, and the atomic number, quality and the thickness of the absorbing sample. The observation of this effect has been reported earlier [23]. Knowledge of the magnitude of the effect due to fluorescence and scattering is therefore required for the interpretation of measurements, when an accuracy of better than 1% is attempted.

Such knowledge can be obtained from the comparison of the mass attenuation coefficients measured in turn with a number of different apertures. From this comparison, one can determine the absolute values of the fluorescence and scattering contributions to the attenuation measurement.

A theoretical model of the effect has been described [18]. To calculate the secondary photons due to the individual emission and scattering processes of a thin layer of material, we first consider the number of photons removed from the incident beam by each process. While the number of scattered photons equals the number of photons removed from the primary beam due to the corresponding scattering process, fluorescence photons are mainly due to K-shell absorption and can be calculated from the K-shell fluorescence yield. To calculate the fraction of these fluorescence or scattered photons reaching the ion chambers, we then apply suitable geometrical factors representing the apertures, and allow for self-absorption and for the angular distribution of the photons [18].

We did indeed observe significant systematic discrepancies between measurements obtained with the different apertures. We are confident that these discrepancies are due mainly to the effect of scattering and fluorescence, and are not, for example, due to the harmonic content of the beam because we have compared at each energy the data from a single foil. In other words, the details of our data allow us to isolate possible systematics by the uniqueness of their signatures.

Our results are in fact in remarkable agreement with the theoretical model as shown in figure 2. The relative uncertainty in the theoretical calculation is estimated at about 10%–20%, corresponding to an absolute uncertainty in $[\mu/\rho]_{\text{meas}}$ of 0.001% (away from the edge) and up to 0.3% (at the edge) [18].

The magnitude of the effect depends on various factors such as the beam energy, the thickness of the foils and the solid angle defined by the apertures. The systematic shift of the final $[\mu/\rho]_{\text{meas}}$ values due to this effect is the average of the effect predicted by the model for individual measurements at each energy. The per cent shift in $[\mu/\rho]_{\text{meas}}$ is shown in figure 3. The discontinuity of the correction at 40.0 keV seen in figure 3 is due to the much thicker foils used for energies above 40.0 keV [18].

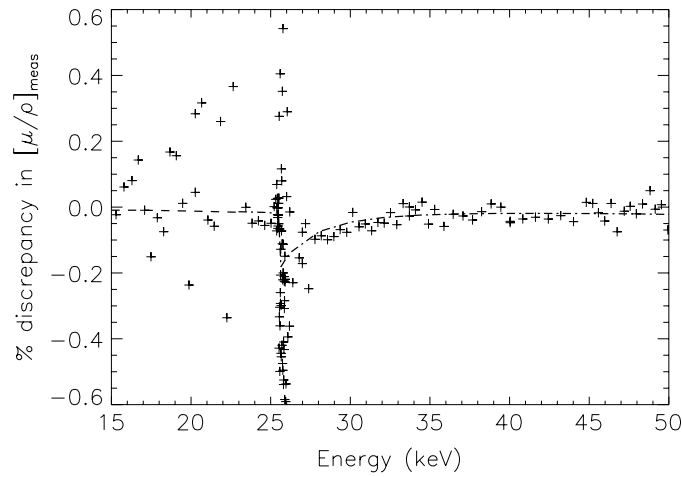


Figure 2. Per cent discrepancy between the mass attenuation coefficients $[\mu/\rho]_{\text{meas}}$ measured with the largest and the medium apertures. The observed discrepancies (+) are compared with a model prediction (dashed line) [18].

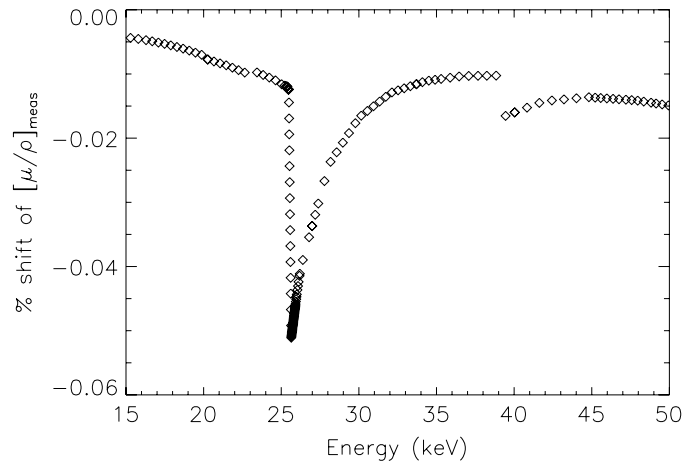


Figure 3. Percentage correction in the measured $[\mu/\rho]_{\text{meas}}$ due to the effect of fluorescence and scattering. The discontinuity in the correction at 40.0 keV is due to the much thicker foils used for energies above 40.0 keV [18].

3.3. Effects due to harmonic contamination and detector nonlinearity

The effect of the presence of a harmonic content in the incident beam on the measurement of the attenuation coefficient depends on (i) the difference between the attenuation of the fundamental and the harmonic components, (ii) the fraction of harmonic photons in the beam and (iii) the relative difference between the detector efficiency for the fundamental and the harmonic energies. The signature of the effect, if significant, can be observed in a comparison of measurements using multiple-foil thicknesses over the entire energy range.

Contributions to the uncertainty of the measurements from the harmonic content of the incident beam and from the non-linearity of the detectors were investigated [25]. In particular, we used two sets of measurements: (i) from the silver foils whose attenuation we measured

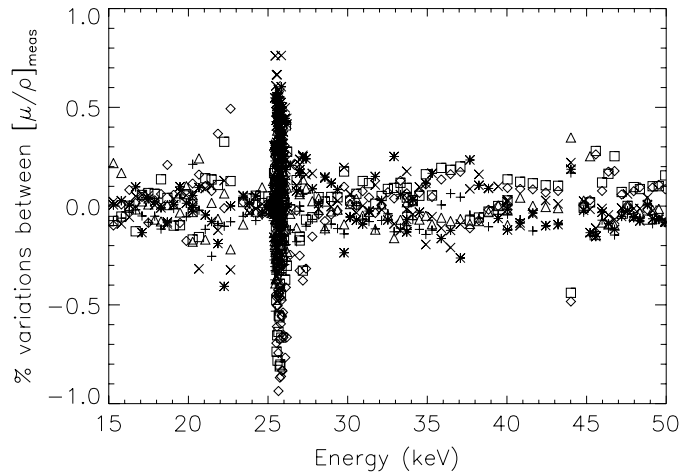


Figure 4. Percentage variations between measurements for all foils and apertures, compared to the average of all measurements at each energy. Most of the data are consistent within $\pm 0.15\%$.

and (ii) from 16 aluminium foils mounted on the downstream daisy wheel whose thicknesses covered an extreme range of attenuations. The significance of the harmonic content and the linearity of the detectors were measured by monitoring the systematic shift in the measured attenuation as a function of the thickness of the absorber.

Figure 4 shows the percentage variations comparing measurements of $[\mu/\rho]_{\text{meas}}$ for all foils and apertures at the same energy. The zero level represents the average of all measurements at each energy. The comparison between the values of $[\mu/\rho]_{\text{meas}}$ shown in figure 4 does not exhibit the signature observable when a significant fraction of harmonic component is present in the beam. Note that the significant systematic discrepancy observed in the K-edge region depends strongly on the aperture sizes, not on the thickness of the foil. As a consequence, this discrepancy at the absorption edge is mainly the signature of the effect of fluorescence and scattering, not of a significant harmonic content in the beam.

A further independent test of the harmonic content of the beam was carried out using the 16 aluminium foils of different thicknesses on the two daisy wheels [25]. Figure 5 shows a result of this test at the lowest nominal energy 15.3 keV at which the harmonic fraction in the incident beam is expected to be the most significant. The linearity of the plot over the $\ln(I/I_0)$ range between 0 and -8 proves that (i) the presence of harmonic components in the beam is insignificant and (ii) the detection system used in the experiment is linear over the attenuation range used ($0.1 < \ln(I_0/I) < 6.8$; see figure 7).

3.4. Energy calibration

The monochromator was moved well above 50 keV and then gradually stepped down in energy during the attenuation measurements to avoid backlash hysteresis [12]. We used an NIST standard Si640b powder sample mounted on the 6-circle Huber stage (figure 1) to measure the energy of the incident beam. The energy measurements were carried out at 46 different energies across the energy range of the measurements.

For each measurement, the angular position of the centroid of each diffraction profile was determined by performing a least-squares fit of the measured profile with a Gaussian curve and a constant background. The measured energy was determined by fitting these

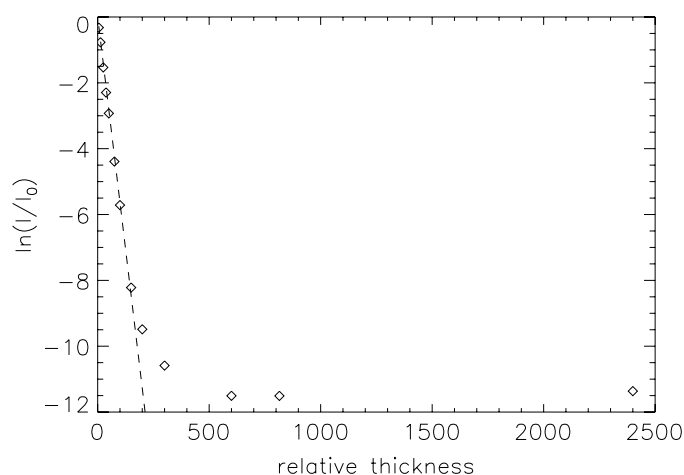


Figure 5. Test of harmonic contribution and detector linearity using the multiple-foil technique. The measurements were obtained at 15.3 keV nominal energy. The linearity of the data indicated by the dashed line is evidence of (i) the excellent linearity of the detection system, (ii) an insignificant presence of harmonic photons over a large attenuation range of $\ln(I/I_0)$ from 0 to -8 .

centroid positions, taking into account the effects of the misalignment of the zero angle of the diffractometer arm and of the powder capillary with the centre of the diffractometer axis [26].

The long-range trends in the directly measured energies were used to calibrate the beam energy as a function of the encoder angle of the monochromator. The interpolation function was based on the Bragg equation with the zero of the monochromator angle and the lattice parameter being allowed to vary slightly from their initial values to account for the monochromator alignment and the expansion of the monochromator crystal under the heat load of the intense synchrotron beam.

The interpolation was divided into two distinct ranges due to an experimental cycling of the monochromator at about 25.2 keV (nominal energy) which resulted in a slight change in the value of the monochromator zero-angle value. Figures 6(a) and (b) show discrepancies between directly measured energies (crosses) and interpolated energies (zero line) in the two ranges. The uncertainty in the energy determination, represented as the envelope, was the standard deviation determined by evaluating the covariant error matrix returned by the (Levenberg–Marquardt least-squares) fitting routine at each interpolated energy.

The final uncertainty of the energy determination Δ_E ranged between 1.6 eV and 4.3 eV, corresponding to between 0.01% and 0.02% for the lower energy region; and between 12.6 eV and 45.7 eV, corresponding to between 0.04% and 0.09% for the higher energy region. The uncertainties in the lower energy region are smaller than those in the higher energy region. The improved stability in the lower energy region is a result of several online optimizations that were carried out while we took data in the higher energy region.

3.5. Statistical errors

The values of $\ln(I_0/I)$ for all foils measured with all three apertures are plotted in figure 7. The foil thickness was chosen such that: (i) where possible, at least one foil was in the optimum statistical range of attenuation ($1 < \ln(I_0/I) < 4$) [27, 20] and (ii) the attenuation range covered by the three foils was as wide as possible, enabling us to probe various sources of systematic errors [21]. The attenuation varied between 0.5 and 5 away from the Ag K-edge,

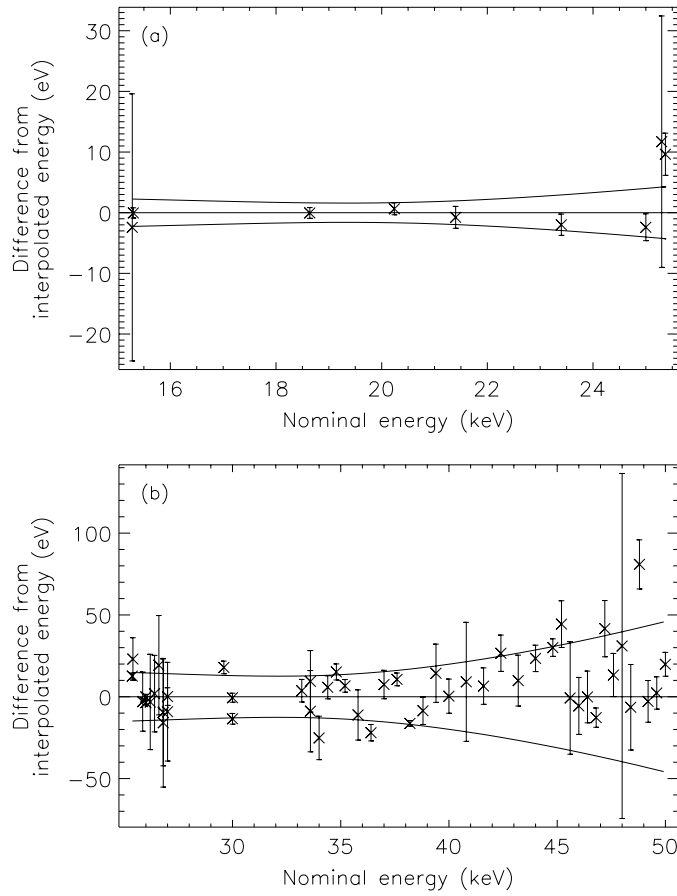


Figure 6. Interpolation of energies for the lower and higher energy ranges (a) and (b). Several online optimizations of the experimental set-up were carried out during the measurements in the higher energy region (b) leading to a much more stable system, including a much better energy determination in the lower energy region (a).

and between 0.1 and 6.8 in the vicinity of the edge. The large attenuation range probed is one of the key features of the XERT for studying significant sources of systematic error affecting the measurement.

Figure 8 shows the percentage uncertainty in $\ln(I_0/I)$ for each foil at each energy due to counting statistics $\% \Delta_{\ln(I_0/I)}$ [20]:

$$\% \Delta_{\ln(I_0/I)} = \frac{\% \Delta_{(I_0/I)}}{\ln(I_0/I)} \quad (2)$$

where

$$\% \Delta_{I_0/I}^2 = \% \Delta_{I_0}^2 + \% \Delta_I^2 - 2R \% \Delta_{I_0} \% \Delta_I. \quad (3)$$

Here R is the correlation coefficient between I and I_0 , and $\% \Delta_{I_0}$ and $\% \Delta_I$ are the percentage uncertainties of the intensities of the incident and attenuated beams.

In most cases, the statistical errors were well below 0.1%. In the low-energy region and in the vicinity of the absorption edge this increased up to 0.15% (for $\ln(I_0/I)$ approaching 6.8) and 0.5% (for $\ln(I_0/I)$ approaching 0.1). However, the final values, being the weighted

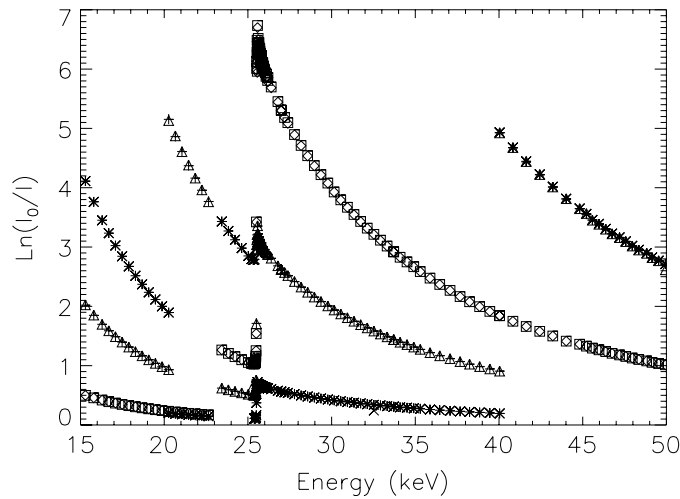


Figure 7. Values of $\ln(I_0/I)$ of three foils measured at each energy. The thicknesses of the three foils were chosen such that (i) a large attenuation range was covered and (ii) where possible, at least one of the three foils had a value of $\ln(I_0/I)$ within the optimum range of counting statistics [27, 20].

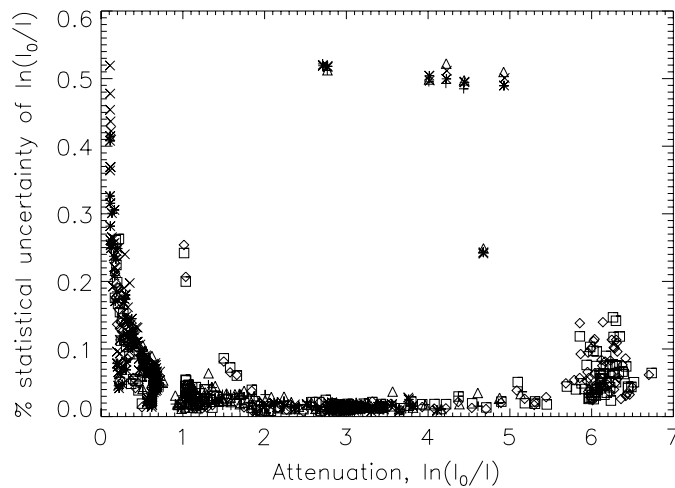


Figure 8. Percentage uncertainty due to the counting statistics of the attenuation measurement, $\% \Delta_{\ln(I_0/I)}$. The attenuation $\ln(I_0/I)$ varied between 0.5 and 5, away from edge, and between 0.1 and 6.8 in the neighbourhood of the absorption edge.

average of the results obtained with the three foils and three apertures, were dominated by measurements obtained with a foil whose thickness corresponded to the optimum statistical range.

The behaviour of $\% \Delta_{\ln(I_0/I)}$ in figure 8 is consistent with a model based on statistical fluctuation only [20]. The small number of inconsistent measurements (whose statistical uncertainty was anomalously high) was due to operational problems.

The plot of the percentage variations in measurements of $[\mu/\rho]_{\text{meas}}$ as shown in figure 4 indicates that the majority of the data are consistent within $\pm 0.15\%$. There are significantly larger variations at the K-edge, and in the 20–23 keV and 44–47 keV ranges. Care must be

taken in considering whether the observed variations in these regions are dominated by noise (in which case the final result of $[\mu/\rho]_{\text{meas}}$ should be the average of all the measurements), or by systematic errors (in which case an appropriate correction should be made to the final $[\mu/\rho]_{\text{meas}}$).

In the energy region between 20 keV and 23 keV, the observed fluctuations are expected to be dominated by counting statistics as the attenuation levels $\ln(I_0/I)$ are not in the optimum statistical range (figures 7 and 8) [20]. Measurements between 44 keV and 47 keV were affected by the electronic settings of the detection system.

In the vicinity of the absorption edge, fluctuations in the individually measured values of $\ln(I_0/I)$ are expected to be enhanced. At the edge even small energy changes lead to significant fluctuations in $[\mu/\rho]_{\text{meas}}$. Also, since in this energy range the attenuation level $[\ln(I_0/I)]$ covers a large range between 0.3 and 6.8, the effect of other systematic errors on the measured $[\mu/\rho]_{\text{meas}}$ is expected to be significant. For example, the effect of fluorescence is strongest in the edge region as the fluorescence production increases as a function of $[\mu/\rho]_K/[\mu/\rho]_{\text{tot}}$ where $[\mu/\rho]_K$ is the photoelectric mass absorption coefficient due to the K-shell electrons.

4. Results and error budget

4.1. Experimental results

Table 3 show the summary of the results. Columns E and Δ_E show the energies (in keV) and the corresponding uncertainties (in eV) at which attenuation measurements were carried out. Columns $[\mu/\rho]_{\text{meas}}$, $\Delta_{\mu,\text{ste}}$ and $\Delta_{[\mu/\rho],\text{meas}}$ show the measured mass attenuation coefficient $[\mu/\rho]_{\text{meas}}$ (in $\text{cm}^2 \text{g}^{-1}$), the weighted deviation and the uncertainties of $[\mu/\rho]_{\text{meas}}$. The uncertainty in the measured mass attenuation coefficient $\Delta_{[\mu/\rho],\text{meas}}$ is the root mean square of the contributions from the uncertainty in the thickness calibration Δ_t and from the consistency of the measurements obtained with the different foils Δ_{ste} :

$$\Delta_{\text{ste}} = \sqrt{\frac{\sum_{\text{all}} \frac{([\mu/\rho]_{t_i} - [\mu/\rho])^2}{\Delta_i^2}}{\sum_{\text{all}} 1/\Delta_i^2}} \quad (4)$$

where $[\mu/\rho]_{t_i}$ are the mass attenuation coefficients measured using foils of different thicknesses t_i , $[\mu/\rho]$ is the weighted average of $[\mu/\rho]_{t_i}$ and Δ_i are the corresponding statistical errors in the measurements of $[\mu/\rho]_{t_i}$.

The column $[\mu/\rho]_{\text{tot}}$ shows the total mass attenuation coefficients obtained by applying appropriate corrections to the $[\mu/\rho]_{\text{meas}}$ for the effects due to fluorescence and scattering. The column σ_{tot} shows the total attenuation cross-sections, obtained from $[\mu/\rho]_{\text{tot}}$ using $\sigma_{\text{tot}}(\text{b/atom}) = [\mu/\rho]_{\text{tot}}(\text{cm}^2 \text{g}^{-1}) \times 1.791 \times 10^2$ [28]. Columns f'' and $\Delta_{f''}$ list the imaginary part of the complex atomic form factor, f , and the corresponding absolute uncertainties. f'' was obtained from the optical theorem:

$$f'' = \frac{\sigma_{\text{pe}}}{2\lambda r_e} = \frac{E\sigma_{\text{pe}}}{2hcr_e} \quad (5)$$

where E is the photon energy, σ_{pe} is the photoelectric absorption cross-section, h and c are Planck's constant and the speed of light, r_e is the classical electron radius, $[\mu/\rho]_{\text{pe}}$ is the photoelectric mass absorption coefficient obtained by subtracting the total scattering coefficients ($[\mu/\rho]_{\text{R}} + [\mu/\rho]_{\text{C}}$) (data taken from [9]) from the total mass attenuation coefficient $[\mu/\rho]_{\text{tot}}$. The use of equation (5) in the region of XAFS (see figure 11) requires further study.

Table 3. Total mass attenuation coefficients $[\mu/\rho]_{\text{tot}}$, total attenuation cross-sections σ_{tot} and the imaginary part of the atomic form factor of silver f'' as a function of energy E , with estimated uncertainties: Δ_E —absolute uncertainty in calibrated energy (one standard deviation); $\Delta_{[\mu/\rho],\text{ste}}$ —percentage precision of repeated measurements (one standard error); $\Delta_{[\mu/\rho],\text{meas}}$ —total percentage accuracy in the measured mass attenuation coefficient $[\mu/\rho]_{\text{meas}}$; f'' —the imaginary part of the complex atomic form factor, obtained using equation (5) where $[\mu/\rho]_{\text{pe}} = [\mu/\rho]_{\text{tot}} - ([\mu/\rho]_{\text{R}} + [\mu/\rho]_{\text{C}})$; $\Delta_{f''}$ —absolute uncertainty in f'' .

E (keV)	Δ_E (eV)	$[\mu/\rho]_{\text{meas}}$ ($\text{cm}^2 \text{g}^{-1}$)	$\Delta_{[\mu/\rho],\text{ste}}$ (%)	$\Delta_{[\mu/\rho],\text{meas}}$ (%)	$[\mu/\rho]_{\text{tot}}$ ($\text{cm}^2 \text{g}^{-1}$)	σ_{tot} (b/atom)	f'' (e/atom)	$\Delta_{f''}$ (e/atom)
15.291	2.3	38.006	0.08	0.28	38.008	6.808×10^3	1.423	0.007
15.791	2.1	34.778	0.07	0.27	34.779	6.230×10^3	1.342	0.007
16.289	2.0	31.915	0.03	0.27	31.916	5.717×10^3	1.267	0.007
16.688	2.0	29.871	0.05	0.27	29.873	5.351×10^3	1.212	0.007
17.087	1.9	27.994	0.06	0.27	27.995	5.014×10^3	1.161	0.007
17.485	1.8	26.283	0.05	0.27	26.284	4.708×10^3	1.113	0.007
17.883	1.7	24.716	0.04	0.27	24.717	4.427×10^3	1.068	0.007
18.280	1.7	23.265	0.07	0.27	23.266	4.167×10^3	1.026	0.007
18.678	1.6	21.944	0.08	0.28	21.945	3.931×10^3	0.987	0.007
19.076	1.6	20.675	0.03	0.27	20.676	3.703×10^3	0.947	0.006
19.473	1.6	19.542	0.07	0.27	19.544	3.501×10^3	0.912	0.006
19.870	1.6	18.489	0.07	0.27	18.490	3.312×10^3	0.879	0.006
20.267	1.7	17.539	0.14	0.30	17.540	3.142×10^3	0.848	0.006
20.267	1.7	17.524	0.02	0.27	17.526	3.139×10^3	0.848	0.006
20.663	1.7	16.592	0.15	0.31	16.594	2.972×10^3	0.816	0.006
21.060	1.8	15.742	0.12	0.29	15.743	2.820×10^3	0.788	0.006
21.457	2.0	14.946	0.12	0.29	14.948	2.677×10^3	0.760	0.006
21.853	2.1	14.210	0.15	0.31	14.211	2.546×10^3	0.734	0.006
22.250	2.3	13.515	0.15	0.30	13.516	2.421×10^3	0.709	0.006
22.646	2.5	12.864	0.20	0.34	12.865	2.304×10^3	0.686	0.006
23.438	3.0	11.717	0.05	0.28	11.718	2.099×10^3	0.643	0.006
23.834	3.2	11.175	0.02	0.28	11.176	2.002×10^3	0.622	0.006
24.230	3.5	10.664	0.04	0.28	10.665	1.910×10^3	0.602	0.006
24.626	3.7	10.190	0.04	0.28	10.191	1.825×10^3	0.583	0.006
25.022	4.0	9.749	0.02	0.28	9.750	1.746×10^3	0.566	0.006
25.219	4.2	9.571	0.02	0.28	9.572	1.715×10^3	0.559	0.006
25.317	4.2	9.523	0.05	0.28	9.524	1.706×10^3	0.558	0.006
25.378	14.8	9.547	0.17	0.40	9.548	1.710×10^3	0.562	0.006
25.383	4.3	9.543	0.03	0.28	9.544	1.710×10^3	0.561	0.006
25.383	4.3	9.552	0.06	0.28	9.553	1.711×10^3	0.562	0.006
25.407	14.8	9.626	0.15	0.39	9.627	1.724×10^3	0.567	0.006
25.427	14.8	9.720	0.18	0.40	9.722	1.741×10^3	0.574	0.006
25.437	14.8	9.788	0.20	0.41	9.789	1.753×10^3	0.579	0.006
25.447	14.8	9.905	0.15	0.39	9.907	1.774×10^3	0.587	0.006
25.456	14.8	10.054	0.29	0.46	10.055	1.801×10^3	0.597	0.006
25.466	14.8	10.295	0.17	0.40	10.296	1.844×10^3	0.613	0.006
25.476	14.8	10.714	0.19	0.40	10.715	1.919×10^3	0.640	0.006
25.486	14.8	11.596	0.20	0.41	11.597	2.077×10^3	0.698	0.006
25.496	14.8	14.277	0.25	0.44	14.279	2.558×10^3	0.874	0.007
25.506	14.8	32.122	1.08	1.14	32.128	5.755×10^3	2.041	0.024
25.516	14.8	56.986	0.31	0.48	56.997	1.021×10^4	3.669	0.018
25.526	14.8	55.765	0.32	0.48	55.778	9.991×10^3	3.590	0.018
25.535	14.8	58.655	0.40	0.53	58.670	1.051×10^4	3.781	0.021
25.545	14.8	60.144	0.25	0.44	60.160	1.078×10^4	3.880	0.018
25.555	14.7	55.361	0.32	0.48	55.377	9.919×10^3	3.568	0.018

Table 3. (Continued.)

E (keV)	ΔE (eV)	$[\mu/\rho]_{\text{meas}}$ ($\text{cm}^2 \text{g}^{-1}$)	$\Delta_{[\mu/\rho], \text{ste}}$ (%)	$\Delta_{[\mu/\rho], \text{meas}}$ (%)	$[\mu/\rho]_{\text{tot}}$ ($\text{cm}^2 \text{g}^{-1}$)	σ_{tot} (b/atom)	f'' (e/atom)	$\Delta f''$ (e/atom)
25.565	14.7	59.342	0.17	0.40	59.361	1.063×10^4	3.831	0.016
25.575	14.7	62.748	0.60	0.70	62.769	1.124×10^4	4.056	0.029
25.585	14.7	57.981	0.17	0.40	58.003	1.039×10^4	3.745	0.016
25.595	14.7	57.038	0.38	0.52	57.060	1.022×10^4	3.684	0.020
25.605	14.7	59.332	0.29	0.46	59.357	1.063×10^4	3.836	0.019
25.615	14.7	60.431	0.22	0.42	60.458	1.083×10^4	3.910	0.017
25.624	14.7	59.705	0.19	0.40	59.733	1.070×10^4	3.864	0.017
25.634	14.7	58.327	0.25	0.44	58.355	1.045×10^4	3.775	0.017
25.644	14.7	58.481	0.34	0.49	58.511	1.048×10^4	3.787	0.020
25.654	14.7	59.420	0.52	0.63	59.450	1.065×10^4	3.850	0.025
25.664	14.7	59.529	0.19	0.40	59.559	1.067×10^4	3.859	0.017
25.674	14.7	58.717	0.35	0.50	58.747	1.052×10^4	3.807	0.020
25.684	14.7	58.474	0.19	0.40	58.503	1.048×10^4	3.792	0.016
25.693	14.7	57.909	0.22	0.42	57.938	1.038×10^4	3.757	0.017
25.703	14.7	57.930	0.19	0.40	57.959	1.038×10^4	3.759	0.016
25.713	14.7	58.591	0.25	0.44	58.620	1.050×10^4	3.804	0.018
25.723	14.7	58.631	0.41	0.54	58.660	1.051×10^4	3.809	0.022
25.733	14.7	58.448	0.41	0.54	58.477	1.047×10^4	3.798	0.021
25.743	14.7	57.720	0.42	0.55	57.749	1.034×10^4	3.751	0.021
25.753	14.7	57.105	0.26	0.44	57.133	1.023×10^4	3.712	0.017
25.763	14.7	57.037	0.23	0.42	57.065	1.022×10^4	3.709	0.017
25.773	14.7	56.895	0.35	0.50	56.922	1.020×10^4	3.701	0.019
25.782	14.6	57.296	0.23	0.42	57.323	1.027×10^4	3.729	0.017
25.792	14.6	57.695	0.20	0.41	57.723	1.034×10^4	3.757	0.016
25.802	14.6	57.654	0.24	0.43	57.682	1.033×10^4	3.756	0.017
25.812	14.6	57.153	0.43	0.56	57.180	1.024×10^4	3.724	0.022
25.822	14.6	56.776	0.21	0.41	56.803	1.017×10^4	3.701	0.016
25.832	14.6	56.120	0.58	0.68	56.147	1.006×10^4	3.659	0.025
25.842	14.6	56.385	0.19	0.40	56.412	1.010×10^4	3.678	0.016
25.852	14.6	56.205	0.29	0.46	56.231	1.007×10^4	3.667	0.018
25.862	14.6	56.183	0.23	0.43	56.209	1.007×10^4	3.667	0.017
25.872	14.6	56.257	0.29	0.46	56.283	1.008×10^4	3.673	0.018
25.882	14.6	56.347	0.35	0.50	56.374	1.010×10^4	3.681	0.019
25.891	14.6	56.507	0.13	0.38	56.534	1.013×10^4	3.693	0.015
25.901	14.6	56.237	0.33	0.49	56.263	1.008×10^4	3.676	0.019
25.911	14.6	56.008	0.17	0.39	56.034	1.004×10^4	3.663	0.016
25.921	14.6	55.707	0.16	0.39	55.733	9.983×10^3	3.644	0.015
25.941	14.6	55.506	0.21	0.41	55.531	9.947×10^3	3.633	0.016
25.961	14.6	55.442	0.28	0.45	55.467	9.935×10^3	3.632	0.017
25.981	14.6	55.516	0.22	0.42	55.541	9.948×10^3	3.640	0.016
26.001	14.6	55.394	0.16	0.39	55.418	9.926×10^3	3.634	0.015
26.040	14.5	54.968	0.16	0.39	54.992	9.850×10^3	3.612	0.015
26.078	14.5	54.607	0.38	0.52	54.630	9.785×10^3	3.593	0.020
26.119	14.5	54.527	0.24	0.43	54.550	9.771×10^3	3.593	0.017
26.179	14.5	53.930	0.32	0.48	53.952	9.664×10^3	3.561	0.018
26.199	14.5	54.056	0.18	0.40	54.078	9.686×10^3	3.573	0.015
26.391	14.4	52.754	0.14	0.38	52.775	9.453×10^3	3.511	0.015
26.791	14.2	50.400	0.10	0.37	50.418	9.031×10^3	3.404	0.014
26.989	14.1	49.224	0.15	0.39	49.240	8.820×10^3	3.348	0.014
27.187	14.0	48.141	0.24	0.43	48.156	8.626×10^3	3.297	0.015
27.187	14.0	47.699	1.08	1.14	47.715	8.547×10^3	3.267	0.038

Table 3. (Continued.)

E (keV)	ΔE (eV)	$[\mu/\rho]_{\text{meas}}$ ($\text{cm}^2 \text{g}^{-1}$)	$\Delta_{[\mu/\rho], \text{ste}}$ (%)	$\Delta_{[\mu/\rho], \text{meas}}$ (%)	$[\mu/\rho]_{\text{tot}}$ ($\text{cm}^2 \text{g}^{-1}$)	σ_{tot} (b/atom)	f'' (e/atom)	$\Delta_{f''}$ (e/atom)
27.385	13.9	47.208	0.16	0.39	47.222	8.458×10^3	3.256	0.014
27.780	13.8	45.346	0.09	0.37	45.358	8.125×10^3	3.172	0.013
28.175	13.6	43.600	0.03	0.36	43.610	7.811×10^3	3.092	0.012
28.571	13.4	42.007	0.10	0.37	42.016	7.526×10^3	3.019	0.013
28.966	13.3	40.453	0.05	0.36	40.462	7.247×10^3	2.947	0.012
29.362	13.1	39.043	0.05	0.36	39.051	6.995×10^3	2.882	0.012
29.757	13.0	37.682	0.15	0.39	37.688	6.751×10^3	2.818	0.012
30.152	12.9	36.353	0.04	0.36	36.359	6.513×10^3	2.753	0.011
30.547	12.8	35.107	0.03	0.36	35.113	6.289×10^3	2.693	0.011
30.942	12.7	33.931	0.07	0.36	33.936	6.079×10^3	2.635	0.011
31.337	12.6	32.809	0.06	0.36	32.814	5.878×10^3	2.580	0.011
31.733	12.6	31.754	0.09	0.37	31.758	5.689×10^3	2.527	0.011
32.128	12.6	30.698	0.03	0.36	30.702	5.499×10^3	2.472	0.010
32.523	12.6	29.719	0.06	0.36	29.723	5.324×10^3	2.422	0.010
32.919	12.6	28.812	0.13	0.38	28.815	5.161×10^3	2.376	0.011
33.313	12.7	27.887	0.10	0.37	27.890	4.996×10^3	2.326	0.010
33.709	12.8	27.013	0.08	0.37	27.016	4.839×10^3	2.279	0.010
33.709	12.8	26.986	0.06	0.36	26.989	4.834×10^3	2.277	0.010
34.104	13.0	26.165	0.04	0.36	26.168	4.687×10^3	2.232	0.010
34.500	13.2	25.432	0.07	0.36	25.435	4.556×10^3	2.194	0.010
34.896	13.4	24.656	0.13	0.38	24.658	4.417×10^3	2.151	0.010
35.290	13.7	23.921	0.09	0.37	23.924	4.285×10^3	2.110	0.009
35.884	14.2	22.869	0.11	0.37	22.871	4.097×10^3	2.049	0.009
36.477	14.8	21.891	0.14	0.38	21.894	3.922×10^3	1.993	0.009
37.070	15.4	20.967	0.14	0.38	20.969	3.756×10^3	1.939	0.009
37.663	16.2	20.054	0.10	0.37	20.056	3.592×10^3	1.882	0.009
38.256	17.0	19.240	0.09	0.37	19.242	3.447×10^3	1.833	0.009
38.849	17.9	18.469	0.06	0.36	18.471	3.309×10^3	1.786	0.008
39.443	18.9	17.724	0.03	0.36	17.727	3.175×10^3	1.739	0.008
40.036	19.9	17.050	0.08	0.37	17.052	3.054×10^3	1.697	0.008
40.036	19.9	17.030	0.02	0.36	17.033	3.051×10^3	1.695	0.008
40.828	21.5	16.168	0.09	0.37	16.171	2.897×10^3	1.639	0.008
41.619	23.1	15.361	0.07	0.36	15.363	2.752×10^3	1.586	0.008
42.411	24.8	14.603	0.06	0.36	14.606	2.616×10^3	1.535	0.008
43.203	26.7	13.881	0.07	0.36	13.883	2.487×10^3	1.485	0.007
43.995	28.6	13.176	0.06	0.36	13.178	2.360×10^3	1.434	0.007
44.787	30.6	12.604	0.02	0.36	12.606	2.258×10^3	1.395	0.007
45.182	31.7	12.300	0.10	0.37	12.301	2.203×10^3	1.373	0.007
45.579	32.7	11.956	0.18	0.40	11.958	2.142×10^3	1.345	0.007
45.975	33.8	11.712	0.07	0.36	11.714	2.098×10^3	1.329	0.007
46.372	34.9	11.426	0.11	0.37	11.427	2.047×10^3	1.307	0.007
46.769	36.1	11.154	0.14	0.38	11.156	1.998×10^3	1.286	0.007
47.164	37.2	10.926	0.04	0.36	10.927	1.957×10^3	1.270	0.007
47.560	38.4	10.692	0.02	0.36	10.694	1.915×10^3	1.252	0.007
47.957	39.6	10.437	0.06	0.36	10.439	1.870×10^3	1.232	0.007
48.353	40.8	10.205	0.06	0.36	10.207	1.828×10^3	1.214	0.007
48.750	42.0	10.004	0.03	0.36	10.006	1.792×10^3	1.199	0.007
49.146	43.3	9.759	0.06	0.36	9.760	1.748×10^3	1.178	0.006
49.531	44.5	9.578	0.08	0.37	9.579	1.716×10^3	1.165	0.006
49.918	45.7	9.381	0.10	0.37	9.382	1.681×10^3	1.150	0.006

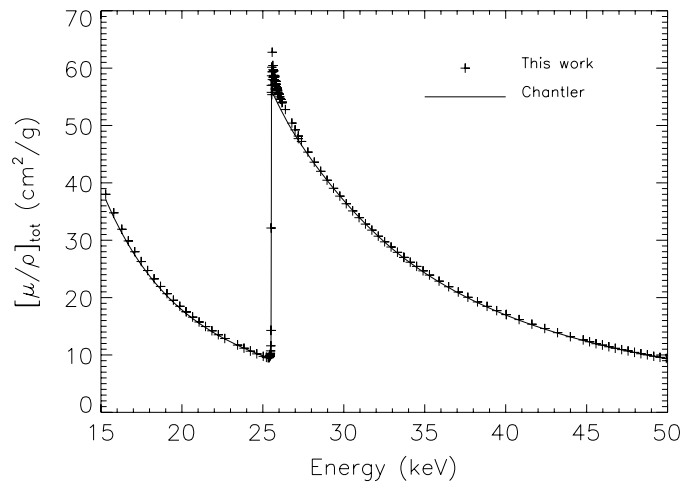


Figure 9. Total mass attenuation coefficients $[\mu/\rho]_{\text{tot}}$ of silver, comparison of the results of this work and theory (Chantler [28, 9]) confirming the broad structure predicted by theory.

The tabulated values of the measured mass attenuation coefficients $[\mu/\rho]_{\text{meas}}$ were calculated from the weighted mean of all the measurements obtained with combinations of the three foils and the three apertures. The total mass attenuation coefficients $[\mu/\rho]_{\text{tot}}$ were obtained by applying appropriate corrections to the measured attenuation coefficients for the effects of scattering and fluorescence (figure 3). As this correction is small (less than 0.05%), the difference between applying this correction before or after taking the average of $[\mu/\rho]_{\text{meas}}$ is insignificant.

Figure 9 shows a comparison between our measurements (weighted average of $[\mu/\rho]_i$ of the three foils plotted in figure 7) and the theory of Chantler [9]. The results confirm the broad structure predicted by theory. Final errors are between 0.27% and 0.4% away from the absorption edge, and up to 0.7% at the edge. This is far better than previous experimental accuracies and is thus capable of differentiating between alternative theoretical predictions (see section 5).

4.2. Summary of uncertainties

Table 4 summarizes the major sources of uncertainty contributing to the tabulated values of $[\mu/\rho]_{\text{meas}}$. Major factors affecting the precision or the consistency of the measurements of $[\mu/\rho]_{\text{meas}}$ using multiple foils are listed as the first two items of table 4. The main factor affecting the measurement consistency are the intrinsic statistics of the system at the level of 0.02% and energy uncertainty.

The final uncertainty in $[\mu/\rho]_{\text{meas}}$ (0.27%–0.4% away from the K-edge, 0.4%–0.7% at the K-edge) is dominated by the experimental precision (0.15% away from the K-edge and 0.2%–0.5% at the edge) and by the uncertainty in the local thickness (0.17%–0.36%).

5. Comparison between theory and experiment

Figure 10 shows the percentage discrepancies in the total mass attenuation coefficients between this work and other experimental, semiempirical and theoretical results, referred to the relativistic Dirac–Hartree–Fock calculation of Chantler [28, 9] (zero line). The two

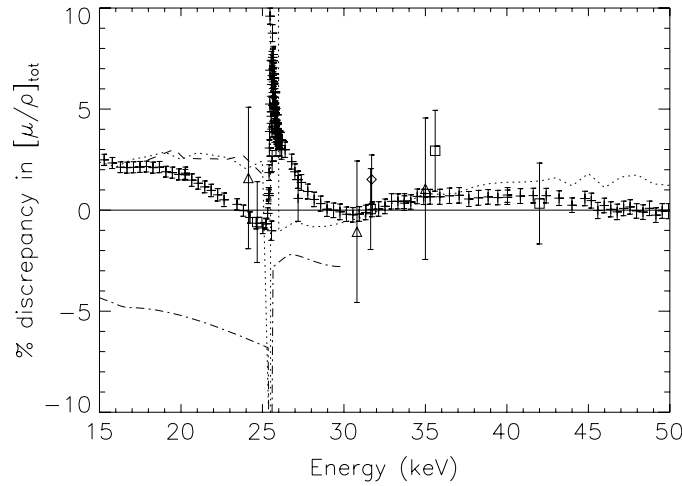


Figure 10. Comparison between $[\mu/\rho]_{\text{tot}}$ of this work and other theoretical, semiempirical and experimental data, $\% \frac{[\mu/\rho]_{\text{tot},i} - [\mu/\rho]_{\text{tot,Chantler}}}{[\mu/\rho]_{\text{tot,Chantler}}}$. Theories include Chantler [28, 9] (zero line), Scofield [29] used by Berger and Hubbell in XCOM [30] (dotted line) and Creagh *et al* [10] (dashed line). Semiempirical tabulation of Henke *et al* [31] (dotted-dashed line) are available up to 30 keV. Other experimental data include those from Machali *et al* [32] (asterisks), Puttaswamy *et al* [33] (diamonds), Santiago and Gowds [3] (triangles) and Visweswara *et al* [34] (squares).

Table 4. Summary of the main sources of uncertainties in the measured mass attenuation coefficient $[\mu/\rho]_{\text{meas}}$.

Source of uncertainty	% contribution		Notes ± 1 standard error
	Away from edge	At the K-edge	
Contributions to precision			
Energy calibration	0.01%–0.02%	0.01%–0.02%	$\Delta_E = 0.007\%–0.08\%$
System statistics	0.02%	0.02%	Reproducibility without sample
Major contributions to accuracy			
Experimental precision	0.05%–0.15%	0.2%–0.5%	Including all above contributions
Sample thickness	0.17%–0.36%	0.17%–0.36%	Thickness calibration and scaling
Minor contributions			
Secondary photons	0.003%	0.01%	20% of the correction (figure 3)
Harmonic contamination	Minor	Minor	
Detector linearity	Minor	Minor	
Additional contributions			
For $[\mu/\rho]_{\text{pe}}$ & $\text{Im}(f)$			
Rayleigh, Compton	Minor	0.05%	
Total final accuracy	0.27%–0.4%	0.4%–0.7%	

theoretical calculations available over the entire energy range between 15 keV and 50 keV are those of Chantler [28, 9] and the nonrelativistic Hartree–Fock–Slater model of Scofield [29] used by Berger and Hubbell in XCOM [30] (dotted line). Data from the relativistic multipole calculation of Creagh and Hubbell [10] (dashed line) are available between 17.44 keV and 24.94 keV. The semiempirical tabulation of Henke *et al* [31] (dotted-dashed line) is available up to 30 keV. Experimental data include those from Machali *et al* [32] (asterisks),

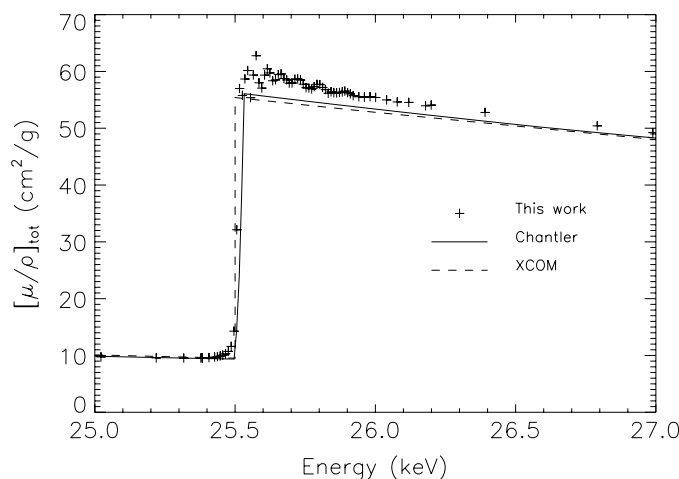


Figure 11. Absolute XAFS of silver compared with the theoretical base lines (Chantler [28, 9], XCOM [30]) which make no allowance for XAFS.

Puttaswamy *et al* [33] (diamonds), Sandiogo and Gowds [3] (triangles) and Visweswara *et al* [34] (squares).

The tabulation from Henke, which is a synthesis between the theoretical input from [29, 35] and experimental data, clearly shows significant discrepancies with other theoretical and experimental data. In the energy region below the K-edge the nonrelativistic calculations from XCOM show excellent agreement with a relativistic calculation of Creagh. However, they are both higher than the relativistic calculation of Chantler by about 2.5%. Above the K-edge, the calculations of XCOM and Chantler agree at the 1% level. However, the XCOM calculation appears to be noticeably higher than that of Chantler towards the high-energy region. Previous experimental results [32, 33, 3, 34] are clearly unable to differentiate between the theories at the 2% level.

No theoretical calculation is in overall agreement with our experimental data within the accuracy of the data. Between 15 keV and 18 keV, there is a good agreement between this work and the theoretical predictions of Creagh and XCOM. However, these theories show a clear overestimation between 18 keV and the K-edge. In contrast, our experimental data show reasonably good agreement with Chantler in the energy range between 23 keV and 25 keV.

Starting from about 28 keV the experimental results fall somewhere between the calculations of Chantler and XCOM. However, beyond about 35 keV these results start to diverge and our measurements develop a trend which results in better agreement with Chantler above 46 keV.

It is interesting to note that the two regions of most significant disagreement with theory occur on the high-energy side of the absorption edge (26–28 keV) and on the low-energy side with a clear trend starting at about 24 keV. A similar discrepancy on the high-energy side of the edge has also been observed in our measurements of copper [12] and the low-energy discrepancy is similar to one observed in silicon [14].

Figure 11 shows the details of the x-ray absorption fine structure (XAFS) of silver comparing it with the theoretical base lines, i.e., the free-atom calculations which are of course not expected to result in absorption fine structure. Our absolute measurements of mass attenuation coefficients exhibit, as would be expected, strong absorption fine structure features. However, these are significantly higher than the base line for several keV—well beyond the

range over which solid-state effects are expected to be significant. We can confidently state this because our measurements are on an absolute scale, unlike conventional XAFS studies in which measurements are on a relative scale which obscures this comparison. Elevated values of the near-edge structure have already been reported in [36] and the possibility of this has also been discussed in previous work; however, here the discrepancy between this work and the theoretical base line is of the order of a hundred standard deviations and therefore is incontrovertible.

6. Conclusion

We have applied the XERT to measure the mass attenuation coefficient of silver in the energy range between 15 keV and 50 keV. All major sources of systematic errors involved in the experiment and known to us have been addressed. Independent thickness determinations have been carried out to confirm the robustness of the technique. The attenuation measurements have, for the first time, been corrected for the effects of scattering and fluorescence.

Acknowledgment

We are grateful for the input and support of the APS staff, especially D J Cookson (Chem-Mat-CARS-CAT) and P L Lee (SRI-CAT). This work was supported by the Australian Synchrotron Research Programme, which is funded by the Commonwealth of Australia under the Major National Research Facilities Programme, and by a number of grants from the Australian Research Council. The use of the advanced photon source was supported by the US Department of Energy, Office of Science, Basic Energy Sciences, under contract no. W-31-109-ENG-38.

References

- [1] Gerward L and Thuesen G 1977 *Z. Naturforsch* a **32** 588
Gerward L, Thuesen G, Jensen M S and Alstrup I 1979 *Acta Cryst. A* **35** 852
Gerward L 1981 *J. Phys. B: At. Mol. Phys.* **14** 3389
Gerward L 1989 *Acta Cryst. A* **45** 1
- [2] Kerur B R, Thontadarya S R and Hanumaiah B 1991 *Appl. Radiat. Isot.* **42** 571
- [3] Sandiogo T K U and Gowda R 1997 *Pramana* **48** 1077
- [4] Wang D, Ding X, Wang X, Yang H, Zhou H, Shen X and Zhu G 1992 *Nucl. Instrum. Methods B* **71** 241
Wang D, Luo P-A and Yang H 1995 *Nucl. Instrum. Methods B* **95** 161
- [5] Baltazar-Rodrigues J and Cusatis C 2001 *Nucl. Instrum. Methods B* **179** 325
- [6] Mika J F, Martin L J and Barnea Z 1985 *J. Phys. C* **18** 5215
- [7] Creagh D C and Hubbell J H 1990 *Acta Crystallogr. A* **43** 102
Creagh D C and Hubbell J H 1990 *Acta Crystallogr. A* **46** 402
- [8] Hubbell J H 1999 *Phys. Med. Biol.* **44** R1–22
- [9] Chantler C T 2000 *J. Phys. Chem. Ref. Data* **29** 597
Chantler C T, Olsen K, Dragoset R A, Kishore A R, Kotochigova S A and Zucker D S 2003 *X-Ray Form Factor, Attenuation and Scattering Tables* (version 2.0) online at <http://physics.nist.gov/ffast>
- [10] Creagh D C and Hubbell J H 1995 *International Tables for X-Ray Crystallography* vol C, section 4.2.4 ed A J C Wilson (Dordrecht: Kluwer)
- [11] Chantler C T 2004 *J. Phys. Chem. Solids* **65** 1935
- [12] Chantler C T, Tran C Q, Barnea Z, Paterson D, Cookson D J and Balaic D X 2001 *Phys. Rev. A* **64** 62506
- [13] Chantler C T, Tran C Q, Paterson D, Cookson D J and Barnea Z 2001 *Phys. Lett. A* **286** 338
- [14] Tran C Q, Chantler C T, Barnea Z, Paterson D and Cookson D J 2003 *Phys. Rev. A* **67** 42716
- [15] Tran C Q, Chantler C T and Barnea Z 2003 *Phys. Rev. Lett.* **90** 257401
- [16] Lengeler B 1994 *Resonant Anomalous X-Ray Scattering—Theory and Applications* ed G Materlik, C J Sparks and K Fischer (Amsterdam: Elsevier) p 35

- [17] Hubbell J H, Veigele W J, Briggs E A, Brown R T, Cromer D T and Howerton R J 1975 *J. Phys. Chem. Ref. Data* **4** 471
Hubbell J H and Øverbø I 1979 *J. Phys. Chem. Ref. Data* **8** 69
Schaupp D, Schumacher M, Rulhusen P and Hubbell J H 1983 *J. Phys. Chem. Ref. Data* **12** 467
- [18] Tran C Q, de Jonge M D, Barnea Z and Chantler C T 2004 *J. Phys. B: At. Mol. Opt. Phys.* **37** 3163
- [19] Lang J C, Srajer G, Wang J and Lee P L 1999 *Rev. Sci. Instrum.* **70** 4457
- [20] Chantler C T, Tran C Q, Paterson D, Barnea Z and Cookson D J 2000 *X-Ray Spectrom.* **29** 449
Chantler C T, Tran C Q, Paterson D, Barnea Z and Cookson D J 2000 *X-Ray Spectrom.* **29** 459
- [21] Chantler C T, Barnea Z, Tran C Q, Tiller J B and Paterson D 1999 *Opt. Quantum Electron.* **31** 495
- [22] Parrish W, Wilson A J C and Langford J I 1999 *International Tables for X-Ray Crystallography* vol C, section 5.2.10 ed A J C Wilson and E Prince (Dordrecht: Kluwer)
- [23] Chantler C T, Tran C Q, Paterson D, Barnea Z and Cookson D J 2000 *Radiat. Phys. Chem.* **61** 347
- [24] Tran C Q, Chantler C T, Barnea Z and de Jonge M D 2003 *Rev. Sci. Instrum.* **75** 2943
de Jonge M D, Barnea Z, Tran C Q and Chantler C T 2004 *Meas. Sci. Technol.* **15** 1811
- [25] Tran C Q, Barnea Z, de Jonge M, Dhal B B, Paterson D, Cookson D and Chantler C T 2003 *X-Ray Spectrom.* **32** 69
- [26] Chantler C T, Tran C Q and Cookson D J 2004 *Phys. Rev. A* **69** 042101
- [27] Nordfors B 1960 *Ark. Fys.* **18** 37
- [28] Chantler C T 1995 *J. Phys. Chem. Ref. Data* **22** 71
- [29] Scofield J J 1973 *Lawrence Livermore Laboratory LLNL Report UCRI-51326*
- [30] Berger M J and Hubbell J H 1987 *XCOM: Photon Cross Sections Database* (NBSIR 87-3597, NIST)
Berger M J and Hubbell J H 1999 *XCOM: Photon Cross Sections Database* version 1.2 online at <http://physics.nist.gov/xcom>
Transformed to Windows platform by Gerward L, Guilbert N, Jensen K B and Levring H 2004 *Radiat. Phys. Chem.* **71** 653
- [31] Henke B L, Gullikson E M and Davis J C 1993 *At. Data Nucl. Data Tables* **54** 181
- [32] Machali F, Al-Barakati G G, El-Sayed A A and Altaf W J 1987 *J. Phys. F: Met. Phys.* **17** 1279
- [33] Puttaswamy K S, Gowda R and Sanjeevaiah B 1981 *Can. J. Phys.* **59** 22
- [34] Visweswara Rao V, Shahnawaz and Venkateswara Rao D 1981 *Physica c* **111** 107
- [35] Saloman E B, Hubbell J H and Scofield J H 1988 *At. Data Nucl. Data Tables* **38** 1
- [36] Del Grande N K 1986 X-ray Imaging II *Proc. SPIE* **691** 2